ACS OMEGA

Open Access

http://pubs.acs.org/journal/acsodf

Article

Impact of FeS on the TiO_2 Layer As Support System in QDSCs

Edson L. Meyer and Mojeed A. Agoro*

Cite This: *ACS Omega* 2024, 9, 37891−37900

Read Online

ACCESS | Metrics & More | Article Recommendations

ABSTRACT: We report on the passivation of titanium oxide with FeS from three molecular precursors with tin sulfide (SnS) photon absorbers that were fabricated and assembled to increase the performance of quantum dot sensitized solar cells (QDSSCs). FeS was loaded on the TiO_2 surfaces, and then, SnS photosensitizer was deposited to form a ternary modified device. The morphology, structural structure, size distribution, chemical composition, and conversion efficiency were explored by FE-SEM, XRD, TEM, UV−vis, EDS, EIS, and J−V analysis. The CV, LSV, and stability state were also investigated for migration and separation of photo-generated charge carriers in the as-prepared cells labeled F-S-1, F-S-2, and F-S-3. The FE-SEM image of the F-S-2 cell is composed of FeS interconnected with SnS and FeS, which provided paths for electron movement compared with the F-S-1 and F-S-3 devices. The semicircle for the F/S-1 and F/S-3 solar device diameters illustrates that the high-medium frequency regain is greater than that of the F/S-2 device, implying that both cells have charge-transfer impedances and lower contact. Apparently, the F/S-2 device shows superior catalytic activity, which can be linked to the hybridization of TiO_2/FeS/SnS due to the synergistic effect. The F/S-2/S-2l has a maximum efficiency η of 6.73% in comparison to F/S-1 and F/S-3, which have the same conversion efficiency of 3.82%. The results of the F/S-2 device follow a similar trend to the chronoamperometry analysis, CV, and LSV results from this study.

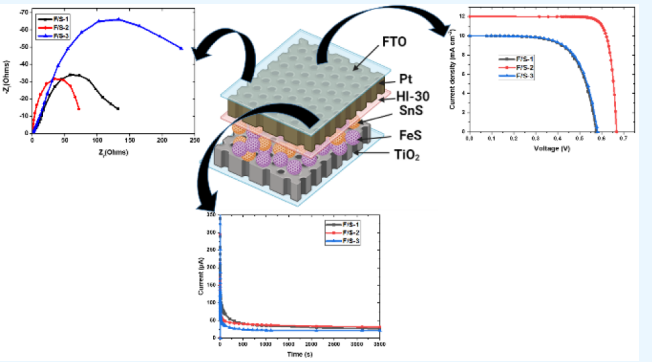

1. INTRODUCTIONS

Global population growth has led to much concern about utilizing and exploiting innovative renewable energies; this has intensified research on solar cells over the past 30 years. Fabrication of more efficient solar cells that are cost-effective and abundant with outstanding potential, such as dye-sensitized solar cells (DSSCs), could be explored.[1−3] The photodegradation issue associated with DSSCs calls for the substitution or discovery of new materials that will improve the device durability and overall performance. The distinct advantages shown by quantum dot-sensitized solar cells (QDSCs), such as easy synthetic route, hot-carrier transfer, optimized optical energy level, low costs, large intrinsic dipole, and high absorption coefficients, place QDSCs as a promising prospective third-generation solar candidate.[4−6] The working mechanisms and architecture of QDSCs are very similar to those of ideal DSSCs, with a simple replacement of organic dyes with a quantum dot (QD) material. QDs have a theoretically estimable efficiency of 44% due to their multiple excitons. Though QDSCs' highest conversion efficiency remains below 13% due to electron loss from photoanode/electrolyte interfaces, transfer at the QD/electrolyte, and charge separation, which is significantly lower than the theoretical estimable value, This is an indication that more study still needs to be done to tackle several factors that influence this poor performance in QDSCs.[7,8] To resolve these issues and improve the performance of QDSCs, major cell structural players such as counter electrodes, nanostructured TiO_2, electrolyte, and semiconductor QDS sensitizer choices should be well considered.

Therefore, passivation or combination of new material on the surface layer of TiO_2 could enhance the electrical equilibrium and the rate of generation of electron holes, resolve QD chemical corrosion, and improve cell stability.[2] Optimization of the metal sulfide band gap using molecular precursors is a promising class of materials for the passivation of the TiO_2 surface layer, which could yield high cell performance. Materials such as SnS_2,[9] FeS, and FeS_2[10,11] have a prominently large surface area with a high performance rate and specific capacities. Iron sulfide is an emerging, newly promising anode material recently considered by several scientists due to its high theoretical capacity, earthly abundance, pollution-free nature, and cost-effectiveness.[12]

Received: May 2, 2024
Revised: June 11, 2024
Accepted: June 14, 2024
Published: August 25, 2024

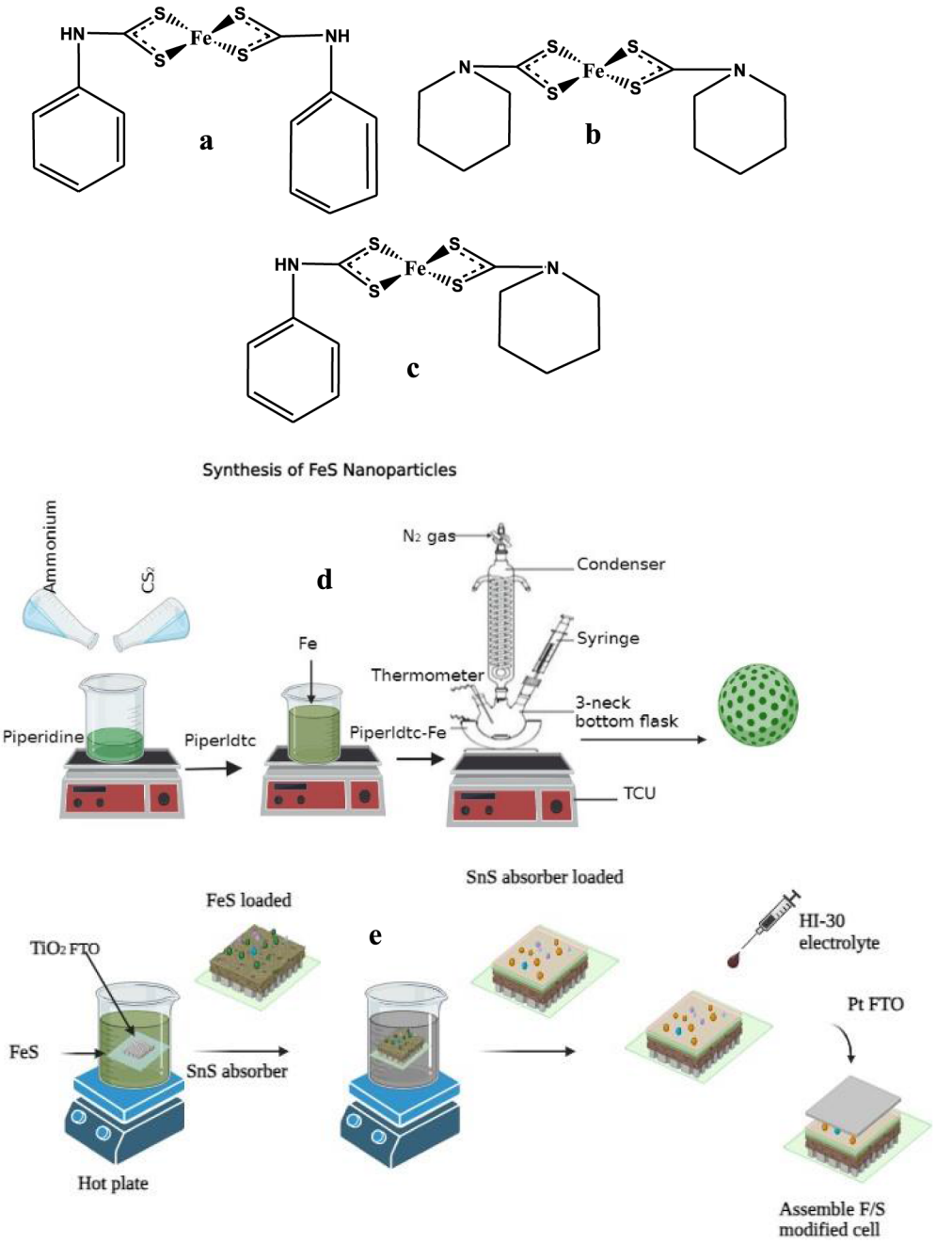

Figure 1. Fe(II) complexes (a−c), synthesis of nanoparticles (d), passivation of synthesized FeS, and assembly of DSSCS (e) for F-S-1, F-S-2, and F-S-3 devices.

Semiconductors FeS and FeS_2 have a narrow band gap of 0.95 eV and a high absorption coefficient ($\alpha > 6 \times 10^5$ cm^{-1} for $h\nu$ > 1.3 eV) as candidates for photosensitization.[13] Song et al.[14] report on photon-induced properties of FeS_2 with TiO_2 nanotube as a photoanode with enhanced photodegradation, and the visible light response of TiO_2 was greatly improved after FeS_2 sensitization.

A substantial study has been piloted to strengthen the photoochemical properties of the transport layer electrode to form heterojunctions via electron transport through doping and the separation of electron−hole and metal nanoparticle loading.[14−16] Among these numerous techniques, metal nanoparticle loading engineering has effectively proven ways to delay the recombination rate and further the transportation of electrons to the participating semiconductor.[14,16] This implies that the choice of absorber materials as a cooperative barrier layer to suppress surface charge recombination is of great importance.[17] A semiconductor photon absorber such as SnS has a high light absorption coefficient that can absorb the entire visible solar spectrum due to its controllable band gap; thus, sensitization of SnS with TiO_2/FeS or TiO_2/FeS_2 having better morphology and optical properties could be the game changer for QDSCs.[14,18] To the best of the authors' knowledge, the metal nanoparticle loading passivation of TiO_2/FeS/SnS in QDSCs has not been extensively studied.

https://doi.org/10.1021/acsomega.4c04226
ACS Omega 2024, 9, 37891−37900

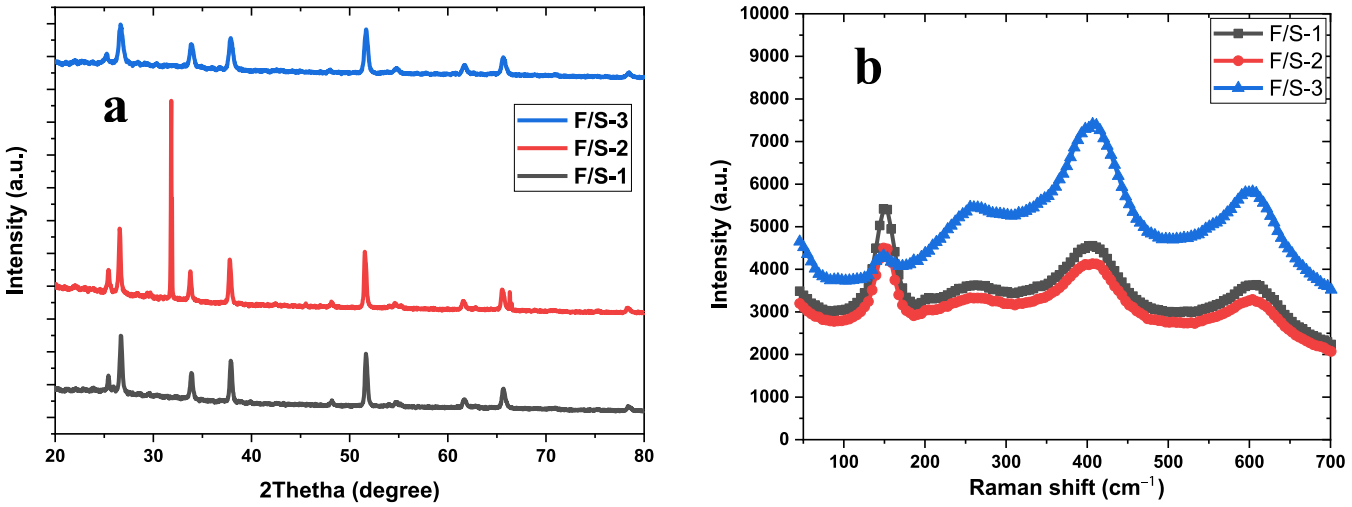

Figure 2. X-ray diffraction patterns (a) and Raman spectra (b) of F-S-1, F-S-2, and F-S-3 thin films.

2. EXPERIMENTAL SECTION

2.1. Materials and Methods. Complete testing kits from Solaronix containing platinum substrate fluorine-doped tin oxide (FTO), TiO_2 substrate (FTO), HI-30 electrolyte iodide, gaskets, masks, and hot seals were purchased. Water, FeS and SnS quantum dots from primary amines Butyldtc and Dodecyldtc Sn(II) complexes and secondary amines form *N*-piperldtc and *N*-anildtc Fe(II) complexes.

2.2. Synthesis, Passivation of FeS, and Assembling of QDSCs. FeS, FeS_2, and FeS metal sulfides were prepared from (*N*-anil-*N*-piperldtc) Fe1), (*N*-piperldtc) Fe2), and (*N*-anildtc) Fe3) as previously reported as FeS#1, FeS#2, and FeS#3.[10] While SnS was formed from [Sn(Dodecbutyldtc)], [Sn(Dodecyldtc)], and [Sn(Butyldtc)]. [Sn(Dodecyldtc)] is labeled as SnS1, SnS2, and SnS3 as seen in Figure 1, as potential photon absorbers, as reported in our previous study.[3] The coating of both materials on the TiO_2 was done by combining the as-prepared FeS#1 with SnS1 and labeling them as F/S-1, FeS#2 and SnS2 as F/S-2, and FeS#3 and SnS3 as F/S-3, respectively. FeS and SnS were used for the passivation and sensitization of the new modified devices in the present study. The TiO_2 substrate was first immersed in 0.1 g of FeS mixed with distilled water for 10 h, then rinsed with distilled water and dried in the air. Subsequently, the coated photoanode substrate was immersed in a 0.1 g SnS solution for 10 h to allow proper sensitization of the TiO_2/FeS.[6] Finally, the coated photoanode substrates were rinsed with distilled water and dried in the air. The photoanodes and the Pt electrodes were sandwiched together using 60 mm thick transparent Surlyn film, and the internal space of the cells was filled with an electrolyte called HI-30. The active area of the solar cells was 0.25 cm^2.

2.3. Physical Characterizations. X-ray diffraction (XRD) patterns of as-prepared devices were identified by using a Bruker D8 Advance A25 system with Cu K$\alpha 1^{+2}$ (λ = 0.154184 nm) radiation at 50 kV and were matched to the reference powder diffraction files (PDFs). The infrared spectra were obtained from the PerkinElmer FT-IR spectrometer at room temperature from a wavenumber of 300 to 4000 cm^{-1}. The optical properties of the three samples were measured through a UV−visible spectrometer via PerkinElmer-Lamda 45. The morphology and size of the fabricated cells were analyzed by a field-emission scanning electron microscope (SEM) using a Nova Nano SEM 430 system and high-resolution transmission electron microscopy (HRTEM) by the JEM-2100F system at 200 kV. The photochemical response of the devices was evaluated by current−voltage (J−V) using a simulated AM 1.5 G solar light radiated by a 550-W xenon lamp solar simulator with incident light intensity at 100 mW/cm^2. The electrochemical impedance spectroscopy (EIS) was analyzed using the Gamry 1010E/ZRA Reference 3000 by a three-electrode standard arrangement consisting of working electrodes, a reference electrode using a saturated calomel electrode, and Pt as the counter electrode. Cyclic voltammetry and chronoamperometry were studied to evaluate the effect of the heterostructure materials on the fabricated devices. Linear scanning voltammetry (LSV) was performed at a scan rate of 10 mV s^{-1}.

3. RESULTS AND DISCUSSION

3.1. XRD. The XRD patterns shown in Figure 2a for the prepared F-S-1, F-S-2, and F-S-3 devices from primary and secondary amine molecular precursors were recorded. The XRD pattern for the three samples matches well with hexagonal FeS (ICDD no. 96−150−4401) and orthorhombic SnS (ICDD no. 96−810−4251). The diffraction peaks could be assigned to (101), (201), (210), (211), (410), (610), and (222) for SnS and (101) for FeS. The parameters of the three samples with passivative layer and photon are tabulated in Table 1, which are in good agreement with previous studies by Malek et al.[19−21] for Fe-doped SnS orthorhombic phase and hexagonal FeS.

The crystal sizes were calculated using the Debye−Scherrer formula:

$$D = \frac{k\lambda}{\beta \cos\theta} \quad (1)$$

where D is the crystal size, k is a constant typically 0.9, λ = 0.15406 nm is the wavelength of the X-ray, β is the fwhm, and θ is the diffraction angle. The average size was 25.14, 22.80, and 38.35 nm for F-S-1, F-S-2, and F-S-3, respectively.

3.2. Raman Analysis. For phase analysis of the F-S-1, F-S-2, and F-S-3 as-prepared electrodes described herein, Raman spectra were obtained and are displayed in Figure 2b. The three prepared cells reveal Raman modes at 158, 204, 260, 415, and 603 cm^{-1}. The modes at positions 158 and 196 cm^{-1} are

https://doi.org/10.1021/acsomega.4c04226
ACS Omega 2024, 9, 37891−37900

Table 1. XRD Parameters for F/S-1, F/S-2, and F/S-3 Devices, Where the Area of Phase A is the (SnS) Peak and the Peak Area of Phase B is (FeS)

no.	2theta [deg]	Miller indices [hkl]	d [Å]	fwhm	matched	D size [nm]
				F/S-1		
1	25.49	(201)	3.4919	0.4200	A	20.26
2	26.51	(210)	3.3593	0.3675		23.21
3	33.70	(101)	2.6571	0.3150	B	27.53
4	37.75	(410)	2.3813	0.3675	A	23.87
5	48.22	(220)	1.8857	0.3675	A	24.75
6	51.53	(610)	1.7722	0.3675	A	25.08
7	65.52	(222)	1.4235	0.3150	A	31.34
						Average 25.14
				F/S-2		
1	20.32		4.3675	1.3650		6.18
2	20.89		4.2481	0.6825		12.37
3	21.79	(101)	4.0760	4.1475	A	2.04
4	25.57	(201)	3.4813	0.2625	A	32.43
5	26.67	(210)	3.3398	0.3150	A	27.08
6	33.86	(211) (101)	2.6451	0.2625	A,B	33.05
7	37.88	(410)	2.3733	0.2625	A	33.43
8	51.63	(610)	1.7688	0.2625	A	35.13
9	65.62	(222)	1.4215	0.4200	A	23.52
						Average 22.80
				F/S-3		
1	25.41	(201)	3.5025	0.2625	A	32.42
2	26.56	(210)	3.3528	0.2625	A	32.49
3	33.76	(101)	2.6531	0.2100	B	41.31
4	37.77	(410)	2.3797	0.2100	A	41.78
5	51.55	(610)	1.7713	0.2625	A	35.12
6	65.52	(222)	1.4235	0.2100	A	47.01
						Average 38.35

similar to the previous studies on hexagonal SnS,[22,23] which established that the modified cells have hexagonal structures. The peaks at 260 and 415 cm^{-1} relate to the characteristic Raman active mode for pyrite (FeS). The vibrational peak at 603 cm^{-1} is assigned to the Ti−O vibrational band contribution. These results prove that the prepared F-S-1, F-S-2, and F-S-3 cells are hexagonal, which could be linked to the miscibility of the metal sulfide at optimized concentration conditions and deposition temperature.[24,25] To identify the possible structural units of the modified cells, FT-IR analysis was used to obtain information about the three samples, as depicted in Figure S1. The broad peaks at 3313 cm^{-1} are observed due to the N−H stretching vibrations. Three bands from 1633−1471 cm^{-1} correspond to the C−N vibration, and the bands at 720 cm^{-1} can be allocated to the C−S vibration. The peaks at 2928 and 2919 cm^{-1} are assigned to the C−H vibration. The M-S bands for the modified cell are found at 580 and 413 cm^{-1} due to Sn−S and Fe−S.[10,26] The presence of all functional groups associated with the metal sulfide confirms the purity of the cells, which correlates with the EDS results.

3.3. TEM, HRTEM, and SAED Analysis. As shown in Figure 3, both HRTEM images (Figure 3c,f,i) and the SAED images (Figure 3b,e,h) do not show clear, sharp diffraction rings. The ring matches well to the indices corresponding to the (101) hexagonal FeS phase, which is similar to the observation by Malek et al.[19] and the (101) orthorhombic SnS phase, as reported by Ning et al.,[27] which correlate with the XRD observation in Figure 2a for the three devices. The diameters of the three samples have a uniform size distribution between 4.12 and 7.82 nm with interplanar distances of 0.33 0.27, and 0.33 nm, which affirms the lattice fringe of (101) hexagonal FeS and (101) orthorhombic SnS.

3.4. SEM and EDS Mapping Analysis. The surface morphology of passivized TiO_2/FeS/SnS modified solar cells derived from molecular precursors was studied using SEM. The SEM images obtained from F-S-1 exhibited spherical and clustered crystallites consisting of irregular nanoparticles, as seen in Figure 4a, and were in good agreement with previous literature[19] for FeS nanoparticles. The F-S-2 metal sulfide is composed of FeS nanoparticles with interconnected SnS balls (Figures 4d,f). Herein, FeS nanoparticles are surrounded by interconnected SnS balls, which are expected to provide paths for electron movement, which cements the strong superiority of the F/S-2 device, which is supported by the study from Li et al.[28] for metal sulfide from molecular precursor. Figure 3g shows that F-S-3 particles are agglomerated and tend to form a rectangular morphology with a nonuniform size distribution. The elemental mapping as shown in Figure 4 (b,c,e,f,h,i-l) confirms the presence of C, O, S, Fe, Sn, and Ti in all three samples, which is similar to the report by Lenus et al.[29] for the elemental confirmation of Fe.

3.5. UV Spectrum and Band Gap Analysis. The optical band gap of the modified cell devices (see Figure 5b) was calculated from the UV−vis data using the formula given below:

$$(\alpha \mathrm{hv}) = A'(E - E_g)^n \quad (2)$$

where A′ is a constant, E_g is the band gap energy, E is the photon energy, α is the absorption coefficient, and n is the power factor of the optical transition mode in a semiconductor, i.e., direct transition ($n = 1/2$). The band gaps of the modified cell devices were obtained by extrapolating the linear portion of the $(\alpha h\nu)^2$ vs E plot for direct transition.

The band gap energy E_g of F/S-1, F/S-2, and F/S-3 cell devices was valued at 3.2, 2.9, and 3.1 eV, respectively. The reduction of E_g implies that there is a reduction in the recombination rate under solar light. The UV−vis spectrum of the three samples, as shown in Figure 5a, shows absorption within the range of 350−400 nm. The F/S-2 heterostructure device displayed significantly enhanced absorption in the visible region compared with the other two samples. These absorptions in visible areas are due to $2(6A_1) \rightarrow (4T_1)$ ligand field transitions of the metal, which collaborate with findings in the literature by Huang et al.[30] for improved photochemical activity and enhanced photogenerated carriers. Tauc plot results are supported by the $J-V$ for the F/S-2 modified device with narrow band gap energy and better conversion output, as also reported by Bootluck et al.[31]

3.6. EIS Nyquist and Bode Plot Analysis. In order to identify the electrochemically prominent properties of F/S-1, F/S-2, and F/S-3 solar cells, readings from electrochemical impedance spectroscopy (EIS) were taken, as illustrated in Figure 6a−c. The fluffy model of the equivalent circuit, signifying the internal resistance of the test cells, was also inserted in Figure 6a−c. The model adopted for the extraction of impedance and the capacitive value are obtained using eq 1, according to the literature by Olayiwola et al.[32,33] This concept is commonly used to explain the occurrence of metal oxide electrodes surface passivation layers, where current must pass

https://doi.org/10.1021/acsomega.4c04226
ACS Omega 2024, 9, 37891−37900

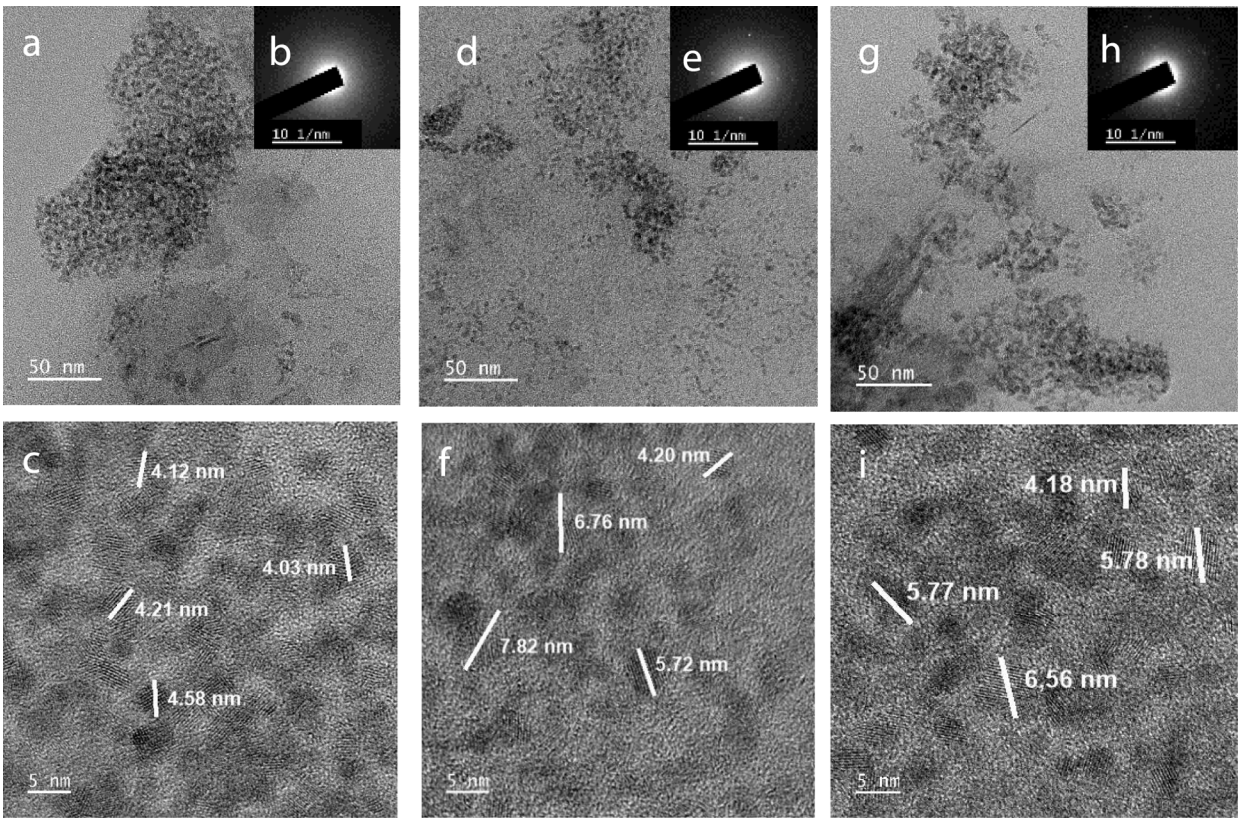

Figure 3. TEM (a–g) and HRTEM (c–i) and SAED (b–h) of F-S-1, F-S-2, and F-S-3 thin films.

through the outer layer before reaching the underlying electrode.

From the Nyquist plots shown in Figure 6, the overall impedance, Z_T, of the devices can be generally considered to be of the form given by eq 3.[32,33]

$$Z_T = R_S + Z_1 + Z_2 \quad (3)$$

Where R_S is the series resistance resulting from the electrode-wafer interface and estimated from the horizontal shift of the impedance from the "origin" = 0 *ohms*. Z_1 represents $R_1 \parallel Z_{CPE1}$ i.e., impedance from the high frequency semicircle of the impedance plot. "CPE" term is used to represent constant phase element for representing an electrochemical element with phase shift starting from +90° to −90°. Thus, it can be used to describe impedance resulting from capacitors (capacitance), resistors (resistance), inductors (inductance), and any other impure element which falls in-between. This is evident as the capacitance measured from the Bode plot is not pure capacitance. However, this value can be converted into a capacitance value and used to obtain the electronic charge-carrier time constant, $\tau_{charge\ carries}$.

Z_2, represents $R_2 \parallel Z_{CPE2}$ or Z_W depending on the Nyquist plot. For cell types F/S-1, F/S-2, and F/S-3, $Z_2 \equiv R_2 \parallel Z_{CPE}$ provides a better description of the chemical process. It should be noted that Z_w describes a much slower charge carrier diffusion as indicated by the arc starting at an approximate angle of 45°. This region of the Nyquist plot is commonly referred to as the Warburg region. The overall diameter of the F/S-3 solar device is significantly larger and illustrates high impedance to carrier mobility compared to that of F/S-1 and F/S-2 device. The values of the intrinsic resistance parameters obtained from equivalent circuit fit using Gamry software are as follows: R_S, R_1, and R_2. R_S 22.42, 16.41, 20.32 Ω, R_1 801.2, 4.225, 896.4 Ω, and R_2 12.15, 6.783, 23.71 Ω. F/S-2 shows both a higher capacitive effect at the low frequency regions of the Bode plot in Figure 6d as well as lower charge delay dynamics at the high frequency region by its lower effective resistance. The behavior of the F/S-2 electrode in the iodolite HI-30 electrolyte depends mainly on the catalytic activity and capacitance of both FeS and SnS synergistic effect on electrode TiO_2/FeS/SnS/iodolyte HI-30. High currents and catalytic electrodes provide low resistance. These results corroborate that the passivation of TiO_2 with the introduction of FeS can improve the electrical conductivity of the overall solar cell TiO_2/FeS/SnS/iodolyte HI-30/Pt for the F/S-2. Figure 6d clearly shows that the introduction of FeS as a passivation layer further decreases the charge transfer resistance and diffusion resistance, which connotes that the ion mobility and conductivity are increasing. Therefore, the electrochemical properties of F/S-2.

3.7. CV Curve and LSV Analysis. The CV curve of the F/S-2 solar cell shows a slight difference in the integrated area compared to the F/S-1 and F/S-3 devices, which connotes the superior electrochemical activity of the F/S-2 modified device, as seen in Figure 7a. This implies that there is a possibility of attaining better photochemical cells through the passivation of TiO_2/FeS/SnS modified devices due to the beneficial synergistic effect. The peak current value for both F/S-1 and F/S-3 modified devices has a capacitance nature.[34] The slight current increase in the F/S-2 device with the injection of HI-30 electrolyte shows a coupled cycling component present (there is a sharp oxidation peak with a significant trailing and a broad reduction peak).[35] Linear sweep voltammetry (LSV) curves representative of F/S-1, F/S-2, and F/S-3 devices are shown in

https://doi.org/10.1021/acsomega.4c04226
ACS Omega 2024, 9, 37891−37900

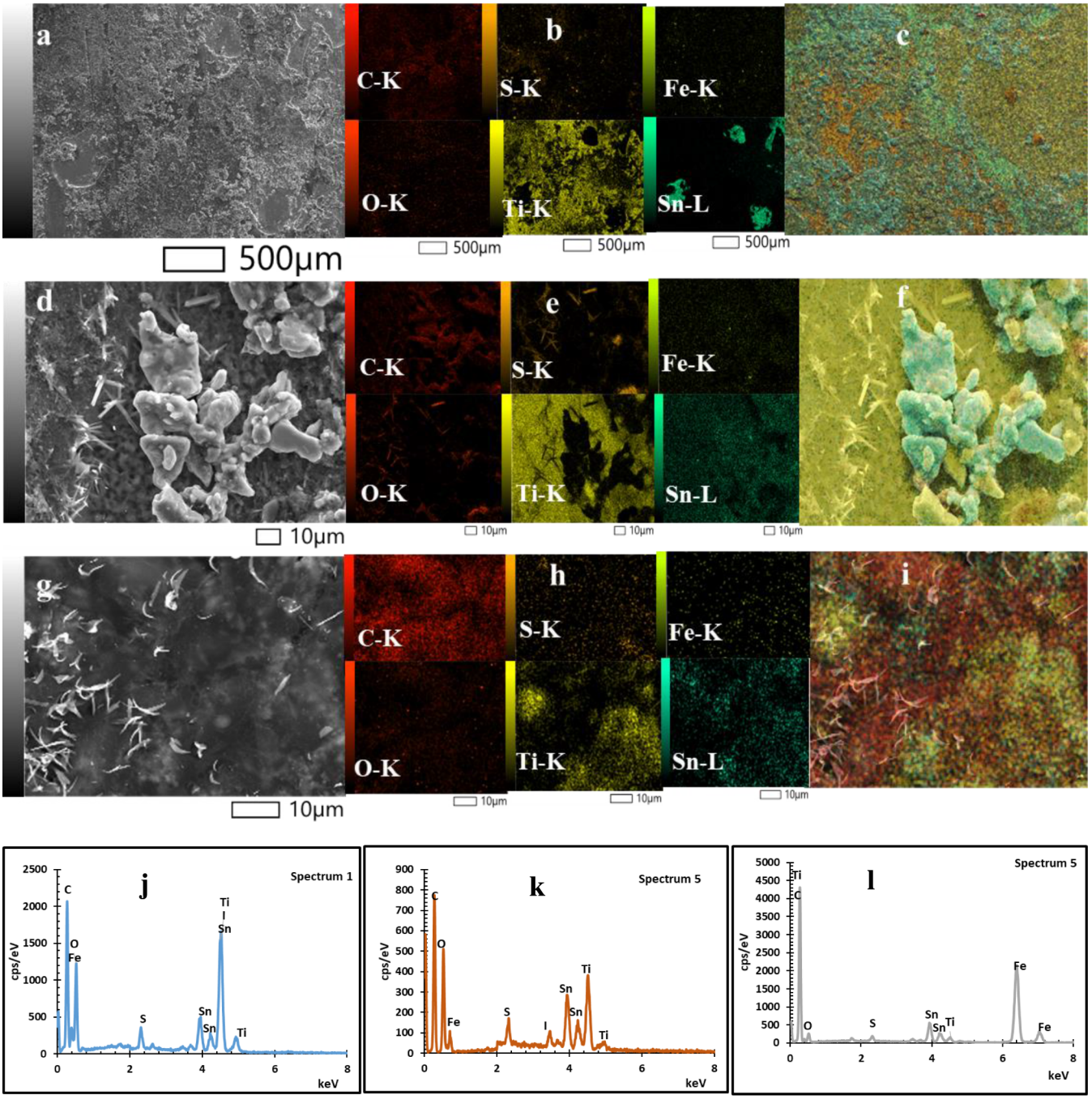

Figure 4. SEM images (a,d,g) and EDS mapping (b,c,e,f,h,i) and spectra (j–l) of F-S-1, F-S-2, and F-S-3 thin films.

Figure 7b. Apparently, the F/S-2 solar device shows superior catalytic activity compared with the F/S-1 and F/S-3 electrodes, illustrating poor catalytic activity. The improved catalytic performance can be linked to the hybridizing of TiO_2/FeS/SnS for F/S-2 due to the synergistic effect, which is supported by Luan et al.[36] and the results of ELS from this study.

3.8. Stability Test and *I*–*V* Curve Analysis. Figure 7c shows the chronoamperometry analysis for the modified hybridized TiO_2/FeS/SnS as F/S-1, F/S-2, and F/S-3 electrode devices using the Cottrell eq 4.

$$I = nFAc_o\sqrt{\frac{D}{\pi t}} \tag{4}$$

Where n is number of electrons transferred, F is Faraday's constant, A is surface area of electrode, C0 is initial concentration, D is diffusion coefficient, and t is time (s). The oxidation current for the F/S-1 and F/S-3 devices decreases rapidly during the initial 300–400 s compared to the F/S-2 within the 100–200 s, which is likely due to the relaxation effects of concentration on the account of diffusional transport of hybridizing SnS/FeS toward the TiO_2 surface before reaching their steady state. The results of the F/S-2 device follow a trend similar to the EIS, CV, and LSV results from this study, with better oxidation current, which coincided with other voltammetry analyses. This further demonstrates the stability of F/S-2 in enhancing the conversion efficiency of the cell. The decrease in F/S-1 and F/S-3 current values could

https://doi.org/10.1021/acsomega.4c04226
ACS Omega 2024, 9, 37891–37900

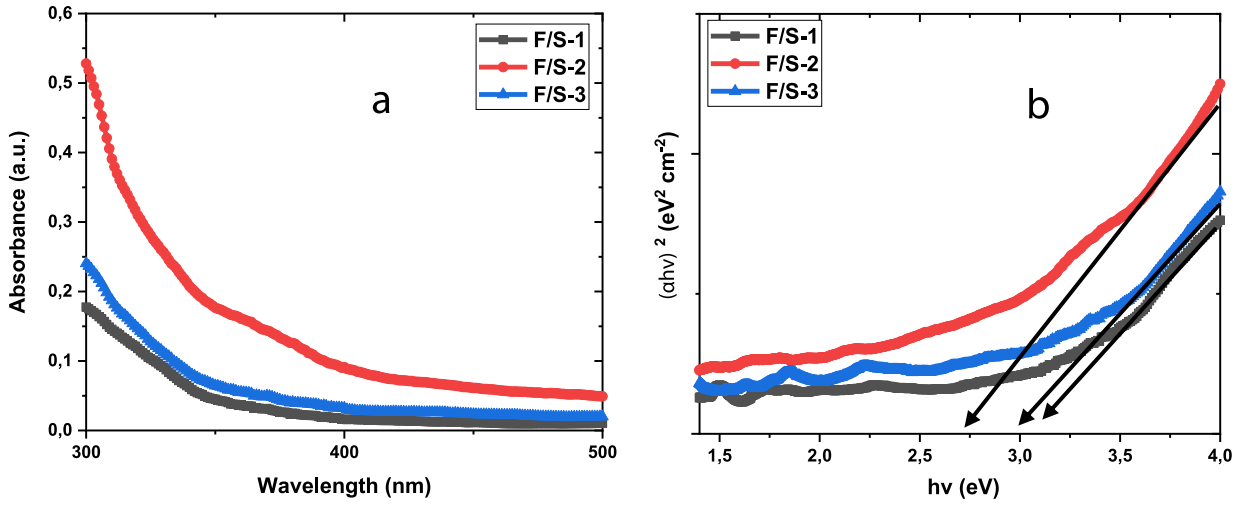

Figure 5. UV−vis absorption (a) and Taucs plot (b) of F-S-1, F-S-2, and F-S-3 thin films.

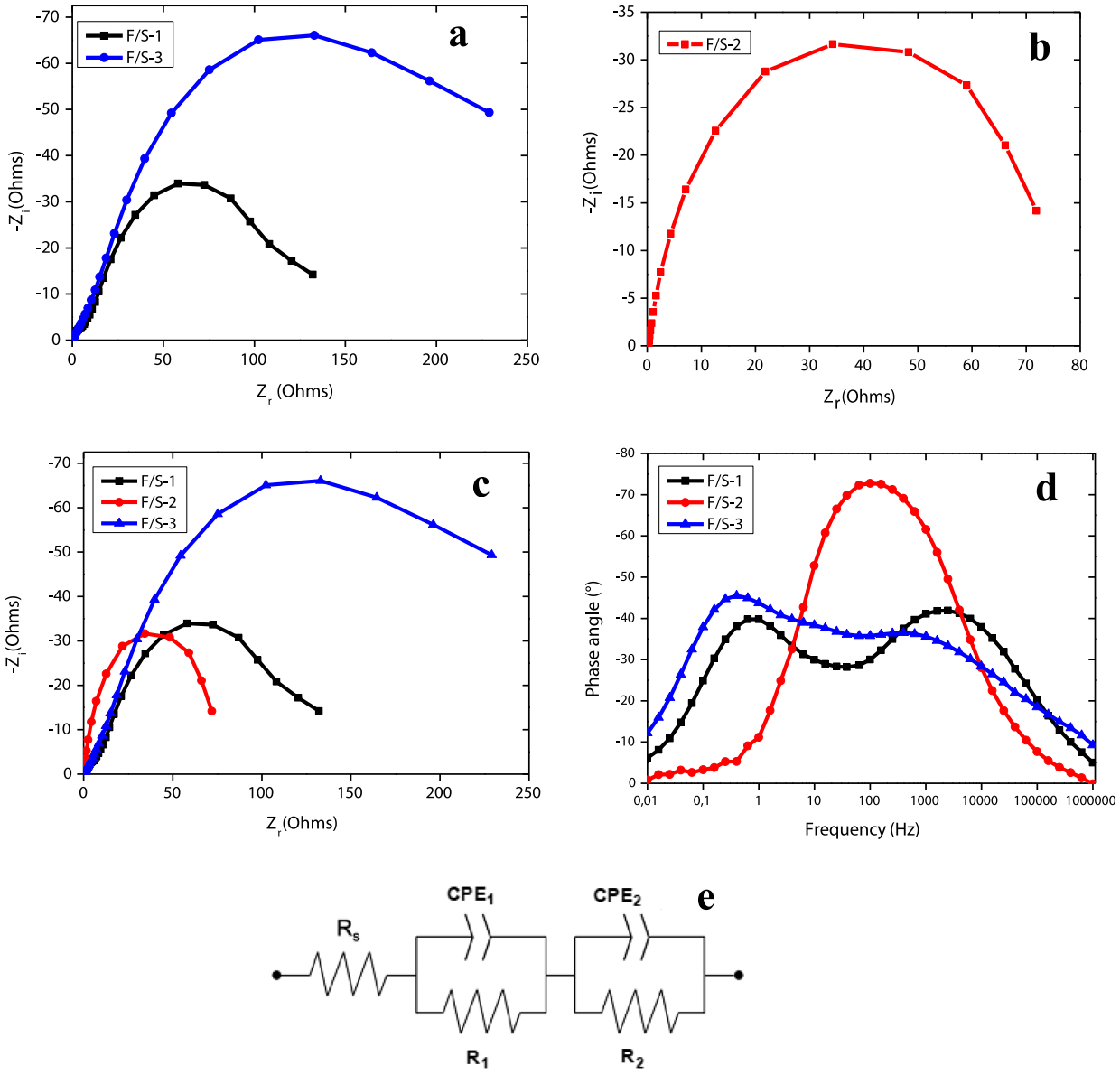

Figure 6. EIS analysis (a−c) and Bode plot (d) of F-S-1, F-S-2, and F-S-3 thin films and the Equivalent circuit model (e).

https://doi.org/10.1021/acsomega.4c04226
ACS Omega 2024, 9, 37891−37900

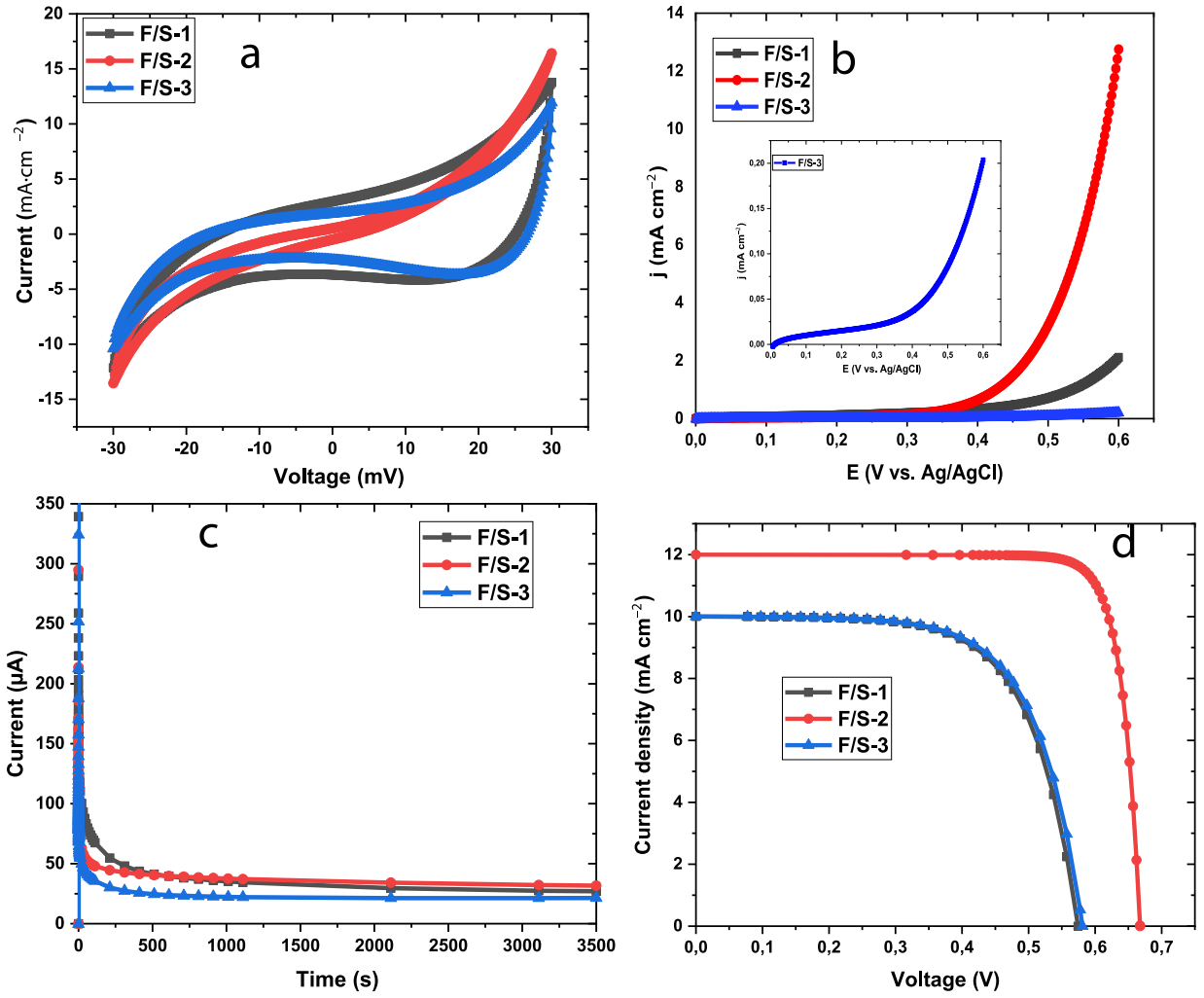

Figure 7. CV curve (a), LSV curves (b), chronoamperograms (c), and *I*−*V* curve (d) of F-S-1, F-S-2, and F-S-3 thin films.

Table 2. *I*−*V* Parameters for F/S-1, F/S-2, and F/S-3 Devices and Previous Studies of QDSCs Passivated Layers[i]

samples	V_{OC} (V)	J_{SC} (mA/cm^2)	*FF*	η (%)	year/ref.
$CuInS_2/ZnS/SiO_2$	0.603	12.83	0.598	4.63	2018[38]
NiS_2 (550°C)	0.45	12.81	42.72	2.25	2018[39]
CuS/NiS	0.45	13.09	0.44	2.56	2018[40]
CuS/CoS	0.56	19.96	0.47	5.22	2018[40]
CuS(1)/CdS(7)	0.65	11.77	0.47	3.60	2015[41]
TiO_2/CdS	0.54	16.07	0.43	3.7	2017[42]
CdS0.12Se0.88	0.56	20.8	0.53	6.14	2018[43]
TiO_2/AISe/CdS/ZnS	0.65	18.27	0.52	6.27	2018[44]
TiO_2/CdS/CdSe	0.62	23.74	0.48	7.16	2018[45]
TiO_2/Cu−In−S	0.64	26.5	0.46	8.0	2018[46]
TiO_2/CdS	0.70	14.05	0.64	6.37	2019[47]
TiO_2/CdSe	0.58	11.83	0.36	2.72	2019[48]
ZnO/TiO_2/CdS	0.46	7.8	0.68	2.44	2020[49]
TiO_2/CdSe	0.48	18.80	0.54	4.88	2021[50]
$NiAl_2O$/CdS/ZnS	0.79	28.22	0.71	15.14	2022[51]
F/S-1	0.57±0.01	10±0.01	0.67±0.02	3.82±0.01	PS
F/S-2	0.66±0.01	12±0.0	0.85±0.02	6.73±0.01	PS
F/S-3	0.58±0.01	10±0.02	0.66±0.0	3.82±0.01	PS

[i]Present study = PS.

be due to decay caused by the instability of the catalyst material and the poisoning of active surface sites. The slow number of active sites accounts for the continuous, slow current time decay. Figure 7d and Table 2 show the *I*−*J* characterization performance parameters, namely fill factor (*FF*), short circuit current (I_{sc}), open circuit voltage (V_{oc}), and

https://doi.org/10.1021/acsomega.4c04226
ACS Omega 2024, 9, 37891−37900

conversion efficiency (η), which were measured and computed according to the eqs and 56.[37]

$$FF = V_m \times I_m / V_{OC} \times I_{SC} \quad (5)$$

$$\eta = V_{OC} \times I_{SC} \times FF \times 100 / P_{input} \quad (6)$$

Table 1 shows that the F/S-2 solar cell has a maximum efficiency η of 6.73% with an increase in the corresponding parameter: V_{oc} at 0.66 V, J_{sc} *at* 12 mA/cm^2, and *FF at* 0.85. Performances of F/S-1 and F/S-3 in Table 2 show that both solar cells are low, having the same conversion efficiency of 3.82%. The poor performance of both devices with semiconductor quantum dot photosensitizers has been attributed to poor interaction passivation of FeS between the TiO_2 surface and the photosensitizer.[37]

4. CONCLUSIONS

In conclusion, the passivated TiO_2/FeS/SnS heterojunctions coupled with a Pt counter electrode were successfully fabricated and assembled in this study in DSSCs. The F/S-3 heterostructure device achieved a significantly enhanced absorption in the visible region. The inclined line from the low frequency affirmed that the diffusion process of the F/S-1 and F/S-3 devices is less difficult, confirming the benefit of passivation on TiO_2 substrate layers with FeS. F/S-2 device's superior catalytic activity was linked to the hybridization of TiO_2/FeS/SnS due to the synergistic effect with maximum efficiency η of 6.73% in comparison to F/S-1 and F/S-3 with 3.82% conversion efficiency. In addition, the chronoamperometry, CV, and LSV results affirm the F/S-2 device as a better photochemical cell.

AUTHOR INFORMATION

Corresponding Author

Mojeed A. Agoro − *Fort Hare Institute of Technology and Department of Chemistry, University of Fort Hare, Alice, Eastern Cape 5700, South Africa;* orcid.org/0000-0002-0434-9635; Email: magoro@ufh.ac.za, amodoyin@gmail.com

Author

Edson L. Meyer − *Fort Hare Institute of Technology, University of Fort Hare, Alice, Eastern Cape 5700, South Africa*

Complete contact information is available at: https://pubs.acs.org/10.1021/acsomega.4c04226

Author Contributions

The authors contributed to the conceptualization, methodology, validation, formal analysis, investigation, resources, data curation, writing of the original draft, review and editing, supervision, and funding acquisition. All authors have reviewed and approved the manuscript.

Funding

The authors acknowledge the financial support received from the PV Spoke National Energy Research Programme of the Department of Science and Innovation, the National Research Foundation (GUN: 137944 and 118 947), and the Govan Mbeki Research and Development Centre (GMRDC) at the University of Fort Hare, South Africa.

Notes

The authors declare no competing financial interest.

ACKNOWLEDGMENTS

The authors appreciate the support from Dr. I.O. Olayiwola, at the Institute for Safe Autonomy University of York, United Kingdom for the EIS data analysis, visualization, review, and editing in the manuscript.

REFERENCES

(1) D'Souza, L. P.; Shwetharani, R.; Amoli, V.; Fernando, C. A. N.; Sinha, A. K.; Balakrishna, R. G. Photoexcitation of neodymium doped TiO_2 for improved performance in dye-sensitized solar cells. *Mater. Des.* **2016**, *104*, 346−354.

(2) Shwetharani, R.; Balakrishna, R. G. One-Pot Synthesis of Flower like FeS_2 as Counter Electrode for Quantum Dot Sensitized Solar Cells. *Mater. Today Proc.* **2019**, *9*, 594−598.

(3) Agoro, M. A.; Meyer, E. L. The formation of SnS nanorods orthorhombic phases grown from different molecular precursors. *Results Chem.* **2023**, *5*, 100690.

(4) Lu, Q.; Li, L.; Xiao, J.; Sui, H.; Li, J.; Duan, R.; Li, J.; Zhang, W.; Li, X.; Kunyang.; et al. Assembly of CdS nanoparticles on boron and fluoride co-doped TiO_2 nanofilm for solar energy conversion applications. *RSC Adv.* **2017**, *7* (46), 29065−29070.

(5) Jiao, S.; Du, J.; Du, Z.; Long, D.; Jiang, W.; Pan, Z.; Li, Y.; Zhong, X. Nitrogen-doped mesoporous carbons as counter electrodes in quantum dot sensitized solar cells with a conversion efficiency exceeding 12%. *J. Phys. Chem. Lett.* **2017**, *8* (3), 559−564.

(6) Agoro, M. A.; Meyer, E. L. Influence of a One-Pot Approach on a Prepared CuS Macro/Nanostructure from Various Molecular Precursors. *Inorganics* **2023**, *11* (7), 266.

(7) Sun, J. K.; Jiang, Y.; Zhong, X.; Hu, J. S.; Wan, L. J. Three-dimensional nanostructured electrodes for efficient quantum-dot-sensitized solar cells. *Nano Energy* **2017**, *32*, 130−156.

(8) Agoro, M. A.; Meyer, E. L.; Mbese, J. Z.; Fuku, X.; Ahia, C. C. Aliphatic mixed ligands Sn(II) complexes as photon absorbers in quantum dots sensitized solar cell. *J. Solid State Chem.* **2022**, *308*, 122890.

(9) Qu, B.; Ma, C.; Ji, G.; Xu, C.; Xu, J.; Meng, Y. S.; Wang, T.; Lee, J. Y. Layered SnS_2-reduced graphene oxide composite−A high-capacity, high-rate, and long-cycle life sodium-ion battery anode material. *Adv. Mater.* **2014**, *26* (23), 3854−3859.

(10) Agoro, M. A.; Meyer, E. L. FeS/FeS_2 nanoscale structures synthesized in one step from Fe(ll) dithiocarbamate complexes as a single source precursor. *Front. Chem.* **2022**, *10*, 1035594.

(11) Hu, Z.; Zhu, Z.; Cheng, F.; Zhang, K.; Wang, J.; Chen, C.; Chen, J. Pyrite FeS_2 for high-rate and long-life rechargeable sodium batteries. *Energy Environ. Sci.* **2015**, *8* (4), 1309−1316.

(12) Cao, Z.; Song, H.; Cao, B.; Ma, J.; Chen, X.; Zhou, J.; Ma, Z. Sheet-on-sheet chrysanthemum-like C/FeS microspheres synthesized by one-step solvothermal method for high-performance sodium-ion batteries. *J. Power Sources* **2017**, *364*, 208−214.

(13) Wang, M.; Qin, H.; Fang, Y.; Liu, J.; Meng, L. FeS_2-sensitized ZnO/ZnS nanorod arrays for the photoanodes of quantum-dot-sensitized solar cells. *RSC Adv.* **2015**, *5* (127), 105324−105328.

(14) Song, X. M.; Wu, J. M.; Meng, L.; Yan, M. Enhanced light response of titania nanotube arrays sensitized with pyrite FeS_2. *J. Am. Ceram. Soc.* **2010**, *93* (7), 2068−2073.

(15) Jayswal, S.; Moirangthem, R. S. Construction of a solar spectrum active SnS/ZnO p−n heterojunction as a highly efficient photocatalyst: the effect of the sensitization process on its performance. *New J. Chem.* **2018**, *42* (16), 13689−13701.

(16) Zhang, X.; Qin, J.; Hao, R.; Wang, L.; Shen, X.; Yu, R.; Limpanart, S.; Ma, M.; Liu, R. Carbon-doped ZnO nanostructures: facile synthesis and visible light photocatalytic applications. *J. Phys. Chem. C* **2015**, *119* (35), 20544−20554.

(17) He, W.; Kim, H. K.; Wamer, W. G.; Melka, D.; Callahan, J. H.; Yin, J. J. Photogenerated charge carriers and reactive oxygen species in ZnO/Au hybrid nanostructures with enhanced photocatalytic and antibacterial activity. *J. Am. Chem. Soc.* **2014**, *136* (2), 750−757.

https://doi.org/10.1021/acsomega.4c04226
ACS Omega 2024, 9, 37891−37900

(18) Xu, Y.; Al-Salim, N.; Tilley, R. D. Synthesis and size dependent reflectance study of water soluble SnS nanoparticles. *Nanomaterials* **2012**, *2* (1), 54−64.
(19) Malek, T. J.; Chaki, S. H.; Giri, R. K.; Deshpande, M. P. The structural, morphological, and optical study of chemical bath deposition and a spin coating deposited mackinawite FeS thin films. *Appl. Phys. A:* **2022**, *128* (9), 830.
(20) Marquez, I. G.; Romano-Trujillo, R.; Gracia-Jimenez, J. M.; Galeazzi, R.; Silva-González, N. R.; García, G.; Coyopol, A.; Nieto-Caballero, F. G.; Rosendo, E.; Morales, C. Cubic, orthorhombic and amorphous SnS thin films on flexible plastic substrates by CBD. *J. Mater. Sci.: Mater. Electron.* **2021**, *32* (12), 15898−15906.
(21) Almanqur, L.; Vitorica-Yrezabal, I.; Whitehead, G.; Lewis, D. J.; O'Brien, P. Synthesis of nanostructured powders and thin films of iron sulfide from molecular precursors. *RSC Adv.* **2018**, *8* (51), 29096−29103.
(22) Chalapathi, U.; Poornaprakash, B.; Park, S. H. Growth and properties of cubic SnS films prepared by chemical bath deposition using EDTA as the complexing agent. *J. Alloys Compd.* **2016**, *689*, 938−944.
(23) Chalapathi, U.; Poornaprakash, B.; Park, S. H. Chemically deposited cubic SnS thin films for solar cell applications. *Sol. Energy* **2016**, *139*, 238−248.
(24) Chalapathi, U.; Poornaprakash, B.; Park, S. H. Effect of post-deposition annealing on the growth and properties of cubic SnS films. *Superlattices Microstruct.* **2017**, *103*, 221−229.
(25) Chalapathi, U.; Poornaprakash, B.; Choi, W. J.; Park, S.-H. Ammonia (aq)-enhanced growth of cubic SnS thin films by chemical bath deposition for solar cell applications. *Appl. Phys. A: Mater. Sci. Process.* **2020**, *126* (8), 583.
(26) Brune, V.; Raydan, N.; Sutorius, A.; Hartl, F.; Purohit, B.; Gahlot, S.; Bargiela, P.; Burel, L.; Wilhelm, M.; Hegemann, C.; et al. Single source precursor route to nanometric tin chalcogenides. *Dalton Trans.* **2021**, *50* (46), 17346−17360.
(27) Ning, J.; Men, K.; Xiao, G.; Wang, L.; Dai, Q.; Zou, B.; Liu, B.; Zou, G. Facile synthesis of IV−VI SnS nanocrystals with shape and size control: nanoparticles, nanoflowers and amorphous nanosheets. *Nanoscale* **2010**, *2* (9), 1699−1703.
(28) Li, C.; Sarapulova, A.; Pfeifer, K.; Dsoke, S. Effect of continuous capacity rising performed by $FeS/Fe_3C/C$ composite electrodes for lithium-ion batteries. *ChemSuschem* **2020**, *13* (5), 986−995.
(29) Lenus, S.; Thakur, P.; Samantaray, S. S.; Narayanan, T. N.; Dai, Z. Two-Dimensional Iron Phosphorus Trisulfide as a High-Capacity Cathode for Lithium Primary Battery. *Molecules* **2023**, *28* (2), 537.
(30) Huang, R.; Liang, R.; Fan, H.; Ying, S.; Wu, L.; Wang, X.; Yan, G. Enhanced photocatalytic fuel denitrification over TiO_2/α-Fe_2O_3 nanocomposites under visible light irradiation. *Sci. Rep.* **2017**, *7* (1), 7858.
(31) Bootluck, W.; Chittrakarn, T.; Techato, K.; Jutaporn, P.; Khongnakorn, W. S-Scheme α-Fe_2O_3/TiO_2 Photocatalyst with Pd Cocatalyst for Enhanced Photocatalytic H_2 Production Activity and Stability. *Catal. Lett.* **2022**, *152*, 2590−2606.
(32) Olayiwola, O. I.; Barendse, P. S. Dynamic equivalent circuit modelling of polycrystalline silicon photovoltaic cells *2017 IEEE Energy Conversion Congress and Exposition (ECCE)*IEEE 2017, 2310−2317. .
(33) Olayiwola, O. I.; Barendse, P. S. Photovoltaic cell/module equivalent electric circuit modeling using impedance spectroscopy. *IEEE Trans. Ind. Appl.* **2020**, *56* (2), 1690−1701.
(34) Huang, Q. H.; Ling, T.; Qiao, S. Z.; Du, X. W. Pyrite nanorod arrays as an efficient counter electrode for dye-sensitized solar cells. *J. Mater. Chem. A* **2013**, *1* (38), 11828−11833.
(35) Karthikeyan, C.; Dhilip Kumar, R.; Anandha Raj, J.; Karuppuchamy, S. One pot and large-scale synthesis of nano-structured metal sulfides: synergistic effect on supercapacitor performance. *Energy Environ.* **2020**, *31* (8), 1367−1384.
(36) Luan, X.; Du, H.; Kong, Y.; Qu, F.; Lu, L. A novel FeS−NiS hybrid nanoarray: an efficient and durable electrocatalyst for alkaline water oxidation. *ChemComm* **2019**, *55* (51), 7335−7338.
(37) Okello, A.; Owuor, B. O.; Namukobe, J.; Okello, D.; Mwabora, J. Influence of concentration of anthocyanins on electron transport in dye sensitized solar cells. *Heliyon* **2021**, *7* (3), No. e06571.
(38) Kim, H. J.; Bae, J. H.; Seo, H.; Shiratani, M.; Venkata Veera Muralee Gopi, C. ZnS/SiO_2 passivation layer for high-performance of $TiO_2/CuInS_2$ quantum dot sensitized solar cells. *Energies* **2018**, *11* (8), 1931.
(39) Gong, C.; Hong, X.; Xiang, S.; Wu, Z.; Sun, L.; Ye, M.; Lin, C. NiS_2 nanosheet films supported on Ti foils: effective counter electrodes for quantum dot-sensitized solar cells. *J. Electrochem. Soc.* **2018**, *165* (3), H45.
(40) Yuan, B.; Duan, L.; Gao, Q.; Zhang, X.; Li, X.; Yang, Y.; Chen, L.; Lü, W. Investigation of metal sulfide composites as counter electrodes for improved performance of quantum dot sensitized solar cells. *Mater. Res. Bull.* **2018**, *100*, 198−205.
(41) Kim, M.; Ochirbat, A.; Lee, H. J. CuS/CdS quantum dot composite sensitizer and its applications to various TiO_2 mesoporous film-based solar cell devices. *Langmuir* **2015**, *31* (27), 7609−7615.
(42) Marandi, M.; Rahmani, E. Optimization of the photoanode of CdS quantum dot-sensitized solar cells using light-scattering TiO_2 hollow spheres. *J. Electron. Mater.* **2017**, *46*, 6769−6783.
(43) Hou, J.; Zhao, H.; Huang, F.; Chen, L.; Wu, Q.; Liu, Z.; Peng, S.; Wang, N.; Cao, G. Facile one-step fabrication of CdS 0.12 Se 0.88 quantum dots with a ZnSe/ZnS-passivation layer for highly efficient quantum dot sensitized solar cells. *J. Mater. Chem. A* **2018**, *6* (21), 9866−9873.
(44) Abate, M. A.; Chang, J. Y. Boosting the efficiency of $AgInSe_2$ quantum dot sensitized solar cells via core/shell/shell architecture. *Sol. Energy Mater. Sol. Cells* **2018**, *182*, 37−44.
(45) Li, Z.; Wang, Y. F.; Wang, X. W.; Yang, Z.; Zeng, J. H. Doping as an effective recombination suppressing strategy for performance enhanced quantum dots sensitized solar cells. *Mater. Lett.* **2018**, *221*, 42−45.
(46) Chiang, Y. H.; Lin, K. Y.; Chen, Y. H.; Waki, K.; Abate, M. A.; Jiang, J. C.; Chang, J. Y. Aqueous solution-processed off-stoichiometric Cu−In−S QDs and their application in quantum dot-sensitized solar cells. *J. Mater. Chem. A* **2018**, *6* (20), 9629−9641.
(47) Zheng, W.; Wang, D.; Wang, Q.; Sun, H. The high performance of quantum dot sensitized solar cells co-sensitized with mixed-joint CdS and ZnS quantum dots. *ECS J. Solid State Sci. Technol.* **2019**, *8* (6), Q96.
(48) Tung, H. T.; Van Thuan, D.; Kiat, J. H.; Phuc, D. H. Ag^+ ion doped on the CdSe quantum dots for quantum-dot-sensitized solar cells' application. *Appl. Phys. A: Mater. Sci. Process.* **2019**, *125* (8), 505.
(49) Tyagi, J.; Gupta, H.; Purohit, L. P. Cascade Structured ZnO/TiO_2/CdS quantum dot sensitized solar cell. *Solid State Sci.* **2020**, *102*, 106176.
(50) Jo, I. R.; Lee, Y. H.; Kim, H.; Ahn, K. S. Multifunctional nitrogen-doped graphene quantum dots incorporated into meso-porous TiO_2 films for quantum dot-sensitized solar cells. *J. Alloys Compd.* **2021**, *870*, 159527.
(51) Mahmoud, S. A.; Elsisi, M. E.; Mansour, A. F. Synthesis and electrochemical performance of α-Al_2O_3 and M-Al_2O_4 spinel nanocomposites in hybrid quantum dot-sensitized solar cells. *Sci. Rep.* **2022**, *12* (1), 17009.

https://doi.org/10.1021/acsomega.4c04226
ACS Omega 2024, 9, 37891−37900